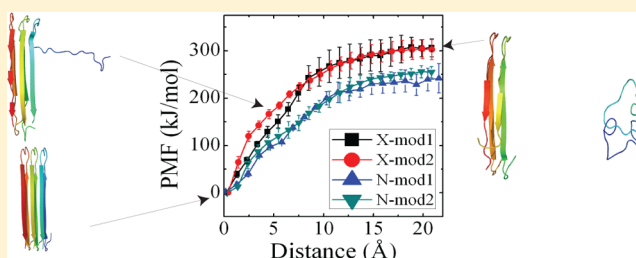


Molecular Dynamics Simulation Study on the Molecular Structures of the Amylin Fibril Models

Weixin Xu,^{†,‡,||,*} Haibin Su,[§] John Z. H. Zhang,^{†,⊥} and Yuguang Mu^{||,*}[†]State Key Laboratory of Precision Spectroscopy, Department of Physics, Institute of Theoretical and Computational Science, East China Normal University, Shanghai 200062, China[‡]Institutes for Advanced Interdisciplinary Research, East China Normal University, Shanghai 200062, China[§]School of Material Sciences, Nanyang Technological University, Singapore 637551[⊥]Department of Chemistry, New York University, New York, New York 10003, United States^{||}School of Biological Sciences, Nanyang Technological University, Singapore 637551

ABSTRACT: The structural characterization of amyloid fibers is one of the most investigated areas in structural biology. Recently, protofibril models for amylin, i.e., the 37-residue human islet amyloid polypeptide or hIAPP were suggested by two groups based on NMR (*Biochemistry* **2007**, *46*, 13505–13522) and X-ray (*Protein Sci.* **2008**, *17*, 1467–1474) techniques. However, there are significant differences in the two models which maybe originate from the polymorphic nature of amylin fibrils. To obtain further insights into the packing and stability features of the different models, we performed a series of molecular dynamics simulations on them. Our analysis showed that even pairs of β -sheets composed of a limited number of β -strands are stable in the 100-ns simulations, which suggests that steric zipper interactions at a β -sheet- β -sheet interface strongly contribute to the stability of these amyloid aggregates. For both models, outer strands are more flexible, which might coincide with the dynamical requirement that outer strands act as growing sites facilitating conformational changes of new incoming chains. Moreover, simulation results showed that the X-ray models are structurally more compact than the NMR models and have more intimate patterns, which lead to more rigid amyloid models. As a result, the X-ray models are energetically more stable than the NMR models. Further modeling analyses verify the most likely amylin fibril model among both NMR and X-ray models. Upon further study of the force-induced dissociation of a single chain from the protofibrils, the binding energy and the mechanical stability of the fibril models are revealed. On these bases, it is possible to reconcile the crystallographic and the NMR data on the basic amylin fiber unit.



I. INTRODUCTION

The 37-residue amylin peptide, also known as human Islet amyloid polypeptide together with α -Synuclein, amyloid β protein, belongs to a group of proteins in which conformational changes of an otherwise soluble peptide lead to refolded/misfolded configurations that in turn aggregate into oligomers, filaments, and ordered fibrils accumulating in plaques in the related organelles.^{1–4}

Intriguingly, the soluble, often globular, precursors of these ordered deposits do not share any sequence/structure similarity. The amyloid fibrils, however, share some common features, like the β strand-loop- β strand motif.⁵ Meanwhile they also commonly exhibit multiple distinct morphologies resolved by electron microscope, atomic force microscope^{6–8} and two-dimensional infrared spectroscopy.⁹ The different fibril morphologies are revealed to have different underlying molecule structures which indicate various assembly behaviors.^{6,10,11}

Amylin fibrils are self-assembled, β -sheet-rich aggregates that typically exhibit diameters in the 5–15 nm range and lengths in

the 0.1–10 nm range. The fibrils are made up of amylin β -strands running perpendicular to the fibril axis, 4.7 Å apart, and are stabilized by hydrogen bonds that run approximately parallel to the fibril axis. The monomeric subunit consists of two β -strands connected by a turn, thus forming a U-shaped topology. Amyloid growth can proceed longitudinally (i.e., the adsorption of new monomers along the fibril axis) and laterally (i.e., the interactions with another stack of monomers at the lateral surface of the growing fiber).^{11–13} Prefibrillar and fibrillar amylin was shown to be toxic to cultured β -cells^{14–18} and has been proposed to play a significant role in the pathogenesis of diabetes II through destruction of β -cells in the later stages of the disease.^{19–24} Knowledge of the detailed molecular structure of amylin fibrils may contribute to the understanding of their cytotoxic properties and development of drugs to prevent the formation of the islet amyloid.^{25,26}

Received: September 2, 2012

Revised: November 13, 2012

Published: November 13, 2012

Recently, molecular structure models for amylin in the fibril form and for the segments of amylin in the protofibril form were resolved by two groups. Tycko and co-workers used scanning transmission electron microscopy and one- and two-dimensional solid-state NMR techniques to obtain constraints on the peptide conformation and supramolecular structure of amylin fibrils. On the basis of these constraints, the authors proposed a single predominant molecular structure of amylin protofilaments in striated ribbons morphology.⁸ Meanwhile, Eisenberg group crystallized two segments from amylin, which themselves form amyloid-like fibrils. The atomic structures of these two segments, NNFGAIL (amylin21–27) and SSTNVG (amylin28–33), were determined, and used in combination with biochemical and structural data from others to propose a structural model of an amyloid fibril of full length amylin.²⁷ It is noted that the NMR and X-ray models have significant structural difference, especially in the side-chain orientation of one β -strand. It is beneficial to understand how the structural differences^{28,29} affect the stability and aggregation pathways^{30,31} of amyloid fibrils.

In this work, we report a series of molecular dynamics simulations of two asymmetric polymorphs of the amylin fibril models (AFMs). The purpose of our study is 3-fold. (1) What are the different structural features of the two AFMs? (2) Which are the most likely models among experimentally proposed AFMs? (3) What is the mechanical stability of the AFMs? Our analysis shows that pairs of β -sheets composed of a limited number of β -strands are stable in the 100-ns trajectories, which suggests that steric zipper interactions at a β -sheet- β -sheet interface strongly contribute to the stability of these amyloid aggregates. For both models, outer strands are more flexible, which might coincide with the structural requirement that outer strands act as growing sites. Moreover, simulation results show that X-ray model is structurally more compact than the NMR model and has a more intimate contacting pattern leading to a more rigid amyloid model. As a result, X-ray model is energetically more stable than NMR model. Further modeling analyses verify the most likely amylin fibril model among both NMR and X-ray models. In addition, upon further study of the force-induced unbinding of monomeric chain from the experimental structures of amylin fibrils, it reveals the mechanical stability of the fibril models.

II. MODEL AND METHODS

A. Simulation Setup and Protocol. In our simulations, amylin fibril subunits were extracted from the 2-fold symmetric model of the amylin fibrils provided by Tycko group (NMR models)⁸ and Eisenberg group (X-ray models).²⁷ Figure 1 shows the two X-ray, (A) X-mod1 (A) and X-mod2 (B), and two NMR, N-mod1 (C) and N-mod2 (D), amylin fibril models. For the two X-ray models, the structural differences locate at the loop region: one spans from Ser19 to Gly24 and the negatively charged His18 is buried inside the loop; while the other spans from Val17 to Gly24 and His18 extends outward. For the NMR models, the major structural differences lie in the orientation of side chains: the side chains of the two models orient in the opposite directions. In addition, NMR and X-ray approaches have yielded similar models. The principal difference between NMR and X-ray structures is that the sheets of the Tycko model do not interdigitate as closely as the Eisenberg model. And the second main difference is in the registration of the two inner sheets. In short, the NMR and X-

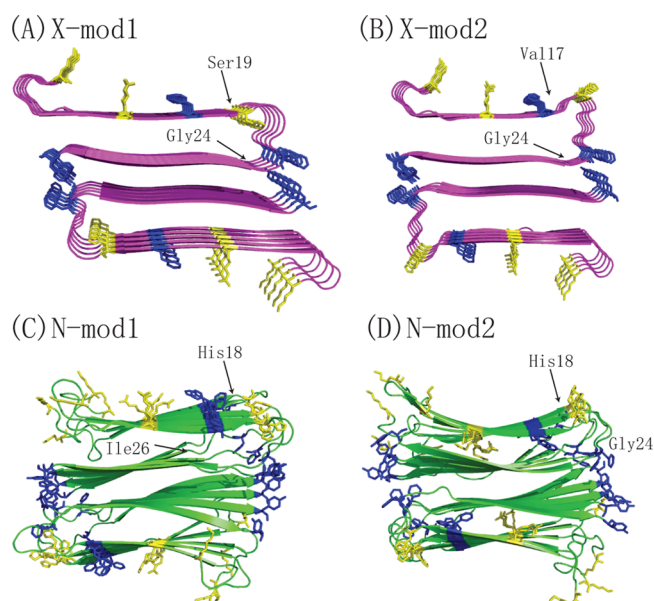


Figure 1. Molecular structural models for the protofilament in amylin fibrils. Cartoon representation of (A) X-ray model I. (B) X-ray model II. (C) NMR model I. (D) NMR model II.

ray structures differ primarily in the details of the packing of side chains.

The sequence of amylin1–37 peptide is KCNTATCATQRLANFLVHSSNNFGAILSSTNVGSNTY. One amylin fibril subunit consists of two layers of antiparallel β -sheets, with each layer containing 5 amylin1–37 peptide chains (see Figure 1). The interface of the two layers is formed by steric zippered side chains. Each peptide is folded in a β -strand-loop- β -strand/U configuration, taking the X-mod1 as an example, an N-terminal β -strand (residues 6–19), a loop (residues 20–23) and a C-terminal β -strand (residues 24–36). We also employed the same conformation in modeling another amylin fibril subunit containing only 3 peptide chains in one layer. For simplicity, we use the following nomenclature for the two amylin fibril subunits: AFS5 and AFS3, respectively. The two amylin fibril subunits were represented by all-atom OPLS force field³² and solvated by explicit SPC water molecules. AFS5 was solvated in a dodecahedron box while AFS3 was solvated in a cubic box. Here a cubic box was used for the sake of convenience and tractability in pulling simulations. For X-mod1, the two final simulation systems contain 10 amylin1–37 peptide chains and 17833 water molecules, 30 chloride ions for the case of AFS5, while 6 amylin1–37 peptide chains and 16890 water molecules, 9 chloride ions for the case of AFS3. All other details are listed in Table 1.

The GROMACS program suite 4.0.3³³ were used. All bonds involving hydrogen atoms were constrained in length according to LINCS protocol.³⁴ Electrostatic interactions were treated with particle mesh Ewald method³⁵ with a real space cutoff of 0.9 nm, and a cutoff of 1.4 nm was used in the calculation of van der Waals interactions. The integration time step of simulation was set to 0.002 ps. The protein and the water groups were separately coupled to an external heat bath with a relaxation time of 0.1 ps. Nonbonded pair lists were updated every five integration steps (0.01 ps). To study the stability of the amylin fibril model, a 50 or 100 ns long molecular dynamics (MD) simulations at 300 K was performed for AFS5. The

Table 1. Summary of Simulated Configurations^a

unit	system	method	sim. time (ns)	sim. no.
X-mod1	10 amylin + 17833 SOL + 30 CL-	NMD	50	1
	10 amylin + 17833 SOL + 30 CL-	NMD	100	1
	3 amylin + 16890 SOL + 9 CL-	PMD	20	3
	3 amylin + 16890 SOL + 9 CL-	PMD	80	3
X-mod2	10 amylin + 17812 SOL + 30 CL-	NMD	50	1
	10 amylin + 17812 SOL + 30 CL-	NMD	100	1
	3 amylin + 14755 SOL + 9 CL-	PMD	20	3
	3 amylin + 14755 SOL + 9 CL-	PMD	80	3
N-mod1	10 amylin + 16795 SOL + 30 CL-	NMD	50	1
	10 amylin + 16795 SOL + 30 CL-	NMD	100	1
	3 amylin + 13248 SOL + 9 CL-	PMD	20	3
	3 amylin + 13248 SOL + 9 CL-	PMD	80	3
N-mod2	10 amylin + 17741 SOL + 30 CL-	NMD	50	1
	10 amylin + 17741 SOL + 30 CL-	NMD	100	1
	3 amylin + 13448 SOL + 9 CL-	PMD	20	3
	3 amylin+13448 SOL + 9 CL-	PMD	80	3

^aHere unit refers to the model of monomeric amylin. NMD and PMD denotes the normal molecular dynamics simulation and umbrella pulling molecular dynamics simulation, respectively.

initial conditions for studying the force-induced unbinding of monomeric peptide from AFS3 are listed in Table 1.

The pulling code of GROMACS 4 was applied to run pulling simulations. In the pulling simulations, the initial structures of amylin fibril (AFS3) was truncated from the complete model (AFSS) determined by both X-ray and NMR methods. The pulling was performed by applying a constant force at one outer monomeric chain while the chain on the opposite side was held fixed, and the middle chain was kept free. In the pulling simulations, the center of mass pulling in the Z direction (pull_vec: 0.0 0.0 -1.0) using an umbrella potential with the force constant 10000 (kJ mol⁻¹ nm⁻²) and pulling rate 0.00005 (nm ps⁻¹) was used. For the pull_geometry, pull_dim, pull_pbcatom1, pull_nstxout and pull_nstfout, the parameters of position, Y Y Y, 0, 2, and 2 were used, respectively. In total, 37 pull groups were used that consist of each residue, and the middle residue in the opposite chain (kept fixed) is taken as the reference group. For pull_init, each vector connecting the pull group and reference group is used to match the "position" option chosen for pull_geometry. Thus, the 37 vectors must synchronize with simulation time. The simulation box will be increased in the Z axis to avoid the interactions between the image of the pulling strand and the reference strands, so that protein does not cross the boundaries during dissociation of the monomeric chain.

B. Analysis Method. The DSSP algorithm written by Wolfgang Kabsch and Christian Sander was used to identify secondary structure conformation of proteins.³⁶

The binding energy of the two- β -sheet-layer oligomers can be estimated by

$$\Delta E = E_{\text{complex}} - \sum_{N=1,2} E_{\text{layer}} \quad (1)$$

and E_{complex} and E_{layer} are the energies of two-layer complex and individual β -sheet layer, both consisting of two terms, force field potential energy ($E'_{\text{gas}} = E'_{\text{vdw}} + E'_{\text{elec}}$) calculated by Gromacs package and solvation energy ($E'_{\text{solv}} = E'_{\text{gb}} + E'_{\text{surf}}$) estimated by generalized Born (GB) model in the sander module of AMBER 9.³⁷ The source code of the tleap program was modified to allow the use of OPLS-AA force field. The modified GB model used was developed by A. Onufriev, D. Bashford, and D. A. Case.³⁸

The absolute entropy was estimated by the quasiharmonic analysis or the essential dynamics method.³⁹ Details can be found in the reference.⁴⁰

The shape complementarity at protein–protein interfaces is calculated by the software SC.⁴¹

III. RESULTS

A. Convergence Test. To verify the convergence of each simulation, the secondary structure propensity (SSP) of amylin in the fibril was assessed. The SSP was averaged over 20-ns windows shown in Figure 2. Because of the stability of the fibril

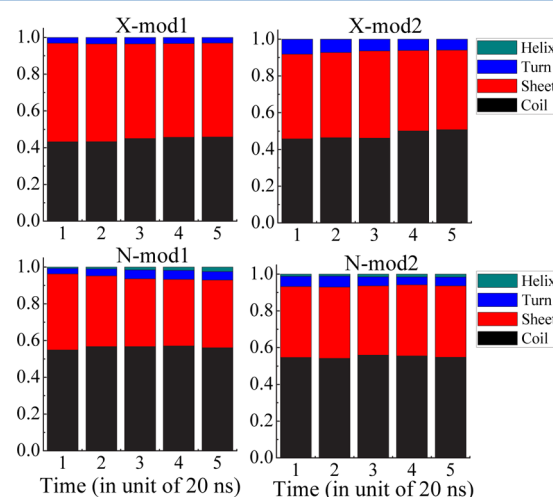


Figure 2. Time evolution of the percentages of residues in Helix, Turn, β -sheet and Coil conformations for simulations of different amylin fibril models.

models, SSP values are slightly changed. From the last 40 ns data, the SSP of two X-ray amylin fibril models (X-mod1 and X-mod2) are quite similar: X-mod1 consists of $\sim 0\%$ helices, 3.1% turns, 51.1% β -hairpins (intra-peptide β -sheets), and 45.8% bend and random coiled structures; X-mod2 consists of $\sim 0\%$ helices, 6.0% turns, 43.3% β -hairpins (intra-peptide β -sheets), and 50.8% bend and random coiled structures.

The SSP of two NMR amylin fibril models (N-mod1 and N-mod2) are also similar: N-mod1 consists of $\sim 2.4\%$ helices, 4.6% turns, 36.9% β -hairpins (intra-peptide β -sheets), and 56.1% bend and random coiled structures; N-mod2 consists of $\sim 1.6\%$ helices, 4.8% turns, 38.8% β -hairpins (intra-peptide β -sheets), and 54.8% bend and random coiled structures. Thus, the structured contents (helices, turns, and β -sheets) contribute, on average, 44.5% and 51.7% for NMR and X-ray models, respectively. Especially, the β -sheet content contributes, on average, 37.8% and 47.2% for NMR and X-ray models, respectively. From the above data, one can clearly see that the structured contents of the NMR models are lower than those of the X-ray models.

B. RMSD and Conformational Entropy. Figure 3 shows the time evolution of root-mean-square deviation (RMSD)

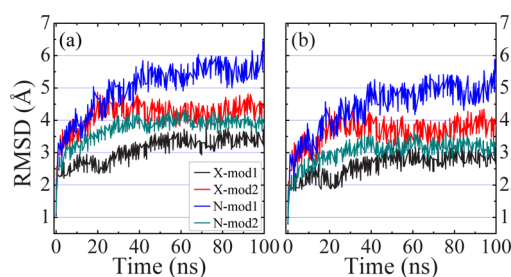


Figure 3. Time evolution of root mean squared deviations (RMSD) for structures of (a) all non-hydrogen atoms and (b) backbone non-hydrogen atoms.

values for both X-ray and NMR amylin fibril models, with respect to the corresponding experimental structures during the molecular dynamics simulations. Here for clarity, the flexible N-terminal (residues 1–8) that is largely exposed to water is removed for the RMSD calculation. Both RMSD values for structures of all non-hydrogen atoms (Figure 3a) and of backbone non-hydrogen atoms (Figure 3b) were calculated. The RMSD reached approximately steady values after about 40 ns, which was mostly less than 4.5 Å based on all non-hydrogen atoms (Figure 3a) or less than 4.0 Å based on backbone non-hydrogen atoms (Figure 3b) for the X-ray models. For one NMR model (N-mod1), the steady RMSD values reached as large as 6.0 Å based on all non-hydrogen atoms (Figure 3a) or 5.0 Å based on backbone non-hydrogen atoms (Figure 3b). Obviously, the average equilibrated RMSD values for X-ray models are smaller than those for NMR models in simulations. On the other hand, for large 10-strand systems like these, RMSD values maintained less than 6 Å during 100 ns trajectories indicate that even pairs of β -sheets composed of a limited number of β -strands are highly stable.

From the RMSD values, it is found that the X-ray models are more rigid, while the NMR models are more flexible. The structural flexibility is also reflected in the entropy. In order to quantitatively characterize the conformational flexibility of both X-ray and NMR amylin fibril models, we checked the time evolution of the conformational entropic⁴⁰ contribution of free energy (here represented by $-TS$) for four trajectories at room temperature (see Figure 4). The entropy contribution becomes nearly constant after about 60 ns sampling. Such an evolution behavior is consistent with the course of RMSD values as shown in Figure 3. Not surprisingly, the absolute entropy contributions from the NMR models are larger than those of the X-ray models. The larger entropy reflects that the NMR

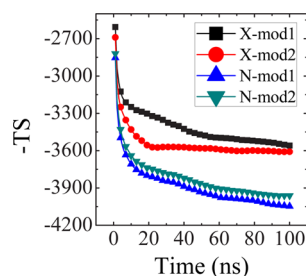


Figure 4. Time evolution of free energy contribution of conformational entropy, $-TS$.

amylin fibril models are more flexible than X-ray models, which is in good agreement with the above analysis.

C. Structural Intimacy and Hydrogen Bond Analysis. It is interesting to check how intimately the different parts in the fibril models interact with each other. Here we investigated the structural complementarity (SC) between two different β sheets. Here the SC value between L1 and L2, between L2 and L3, and between L3 and L4 is denoted as Sc1, Sc0, and Sc2, respectively (see Figure 5). Thus, Sc1 and Sc2 are to describe

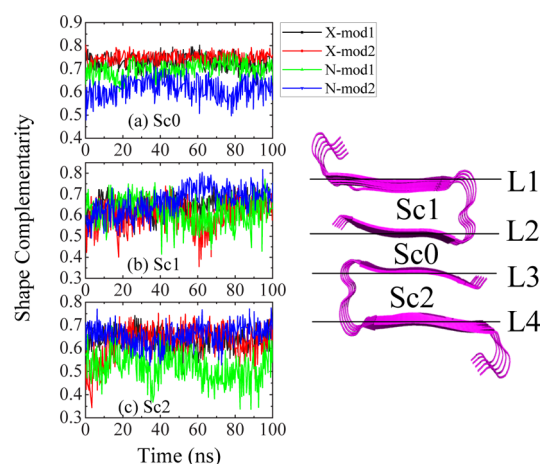


Figure 5. Time evolution of the shape complementarity (a) between layer 2 (L2) and layer 3 (L3), (b) between layer 1 (L1) and L2, and (c) between L3 and layer 4 (L4).

the intrasheet structural complementarity, while Sc0 is to measure the intersheet structural complementarity. Larger SC value means better shape matching between two interacting surfaces, i.e., an intimate interface. As seen from the flat curves in Figure 5a–c, overall these SC values are kept nearly constant during simulations, indicating stable interfaces. It is noted from Figure 5a, the SC values of X-ray models (on average, Sc0 = 0.73 for X-mod1 and 0.75 for X-mod2) are larger than those of NMR models (on average, Sc0 = 0.69 for N-mod1 and 0.62 for N-mod2), suggesting that X-ray models have a more intimate intersheet packing patterns than NMR models. From Figure 5a, one can also note that N-mod1 has a higher intersheet structural complementarity than N-mod2. In addition, the intersheet structural complementarity between L2 and L3 (i.e., Sc0) are generally higher than the intrasheet structural complementarity (i.e., Sc1 and Sc2), except the amylin model of N-mod2. Take the X-mod1 as an example, on average, Sc0 = 0.73 while Sc1 = 0.65 and Sc2 = 0.64. The high values of Sc0 indicates an intimate interface between two amylin β -sheet layers (L2 and L3) that is scaffolded by the steric zipper interactions (as apparently displayed in Figure 8).

The time evolution of the number of in-register interchain backbone (BB) hydrogen bonds (Figure 6a), total interchain backbone hydrogen bonds (Figure 6b) and total hydrogen bonds (Figure 6c) are monitored. Overall, the amount of hydrogen bonds in the X-ray amylin fibril models is significantly larger than that in the NMR models. For example, ~80 and ~65 in-register interchain backbone hydrogen bonds are formed in X-mod1 and X-mod2, respectively. However, there are only ~50 and ~40 in-register interchain backbone hydrogen bonds formed for the N-mod1 and N-mod2, respectively. Clearly, X-ray models have more intramolecular

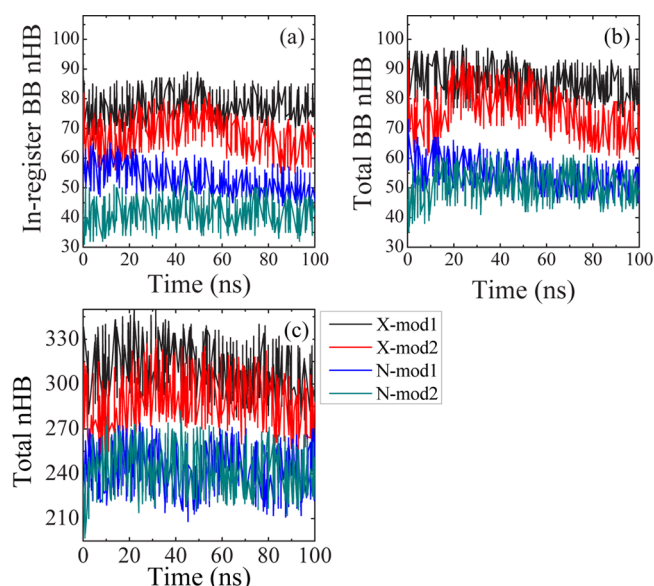


Figure 6. Time evolution of the number of (a) in-register backbone (BB) hydrogen bonds, (b) total backbone hydrogen bonds, and (c) total hydrogen bonds.

interactions than NMR models. That is why X-ray models are more stable than NMR models.

D. Binding Energies. It is also interesting to check the thermostability of these fibril structural models by looking at the binding energies. We calculated the total potential energy and binding energy between two different layers using the generalized Born model implemented in Amber 9 simulation package. To monitor the convergence of energy, we show the time evolutions of the total potential energies of four trajectories at 300 K (see Figure 7a). One can observe that the total potential energy of X-mod1 and X-mod2 is relaxed to a stable value ~ -53868 kJ/mol and ~ -53408 kJ/mol within 40 ns, respectively. While the total potential energy of N-mod1

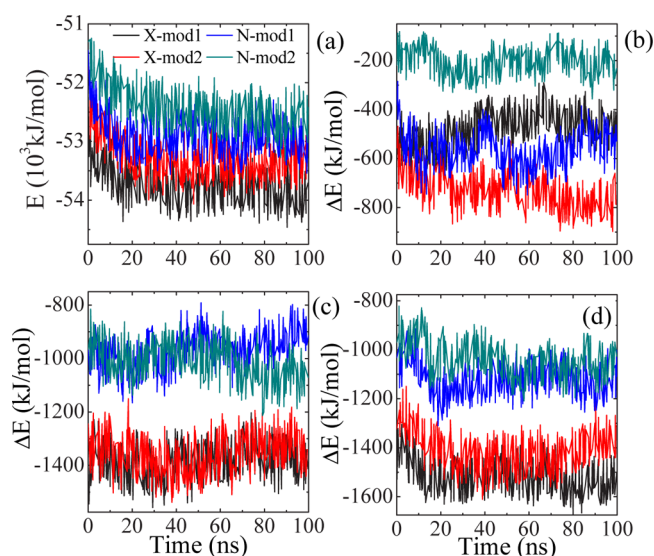


Figure 7. Time evolution of (a) the total potential energies, (b) the interlayer binding energies, (c) the binding energies of internal strands, and (d) the binding energies of outer strands, calculated using the MM-GBSA method for both X-ray and NMR amyloid fibril structure at 300 K.

and N-mod2 is relaxed to a stable value ~ -52911 kJ/mol and ~ -52484 kJ/mol within 40 ns, respectively. Thus, the total potential energies of X-ray amylin fibril models are 940 kJ/mol on average lower than those of NMR models, which suggests that the X-ray amylin fibril models are energetically more stable than the NMR models. We realize that for such large simulation systems, it is hard to get a true equilibrium distributions of conformations. The relatively fast convergence of the total energies, however, provides us an indicator of the relative thermostability of X-ray and NMR amylin fibril models.

The assembly energies of different fibril models were also investigated by calculating the binding energies of two layers and two sheets. Figure 7b shows the binding energies between one layer (upper five strands) and the other layer (lower five strands): two layers, i.e., between L2 and L3 as shown in Figure 5. These two layers are stabilized by the side chain-side chain packing interactions mainly by the van der Waals and electrostatic interactions, forming the steric zipper pattern. The binding energy of X-mod1 and X-mod2 is relaxed to ~ -444 kJ/mol and ~ -741 kJ/mol, respectively. On the other hand, the binding energy of N-mod1 and N-mod2 is relaxed to ~ -550 kJ/mol and ~ -197 kJ/mol, respectively. One can see that, on average, the X-ray model has a lower binding energy.

Further, binding energy between two zippering strands and their adjacent two strands along the fibril growth direction (i.e., the fibril axis) was also calculated for different fibril models. In the case of two outer strands/two neighboring internal strands, the average binding energy profiles are shown in Figure 7c. While for four internal strands, the average binding energy profiles are shown in Figure 7d. Obviously, for both cases, the binding energies of X-ray models are significantly lower than those of NMR models. In addition, the binding energy for four internal strands is slightly (about 100 kJ/mol) lower than two outer strands/two internal strands. This is understandable because outer strands are more flexible than internal strands, which arises in loose structure and higher binding energy with adjacent strands. In contrast, the core of the 3-member cross- β -subunit (consisting of the 3 inner peptides) was very stable, while the 2 outer peptides showed more fluctuations. This is to be expected as the outer peptides have only one neighboring peptide that can provide stabilizing interactions. As examples, we also computed the root-mean-square fluctuation (RMSF, i.e., the standard deviation) of atomic positions after fitting to the initial structure, which was later converted to B-factor value (data not shown). The color on the structure showed that outer strands are relatively more flexible with respect to the internal strands in the amyloid fibril. In addition, it is also noted that the binding energy between two strands and two neighboring strands (see Figure 7c,d) is more than 600 kJ/mol lower than the binding energy between two layers (as shown in Figure 7b). This is due to the strong hydrogen bonding interactions between strands along the fibril growth direction for the former. While the two stacking layers are mainly stabilized by side chain-side chain hydrophobic interactions.

In addition, the breakdown of binding energy components is listed in Table 2. Overall, it is shown that the nonpolar energy contributes dominantly (large negative ΔE_{np}) to the thermostability of these four fibril structural models, while the polar energy (with positive ΔE_p) plays a negative role. This suggests that fibril aggregation is driven by the nonpolar interaction. Among the nonpolar energy, the van der Waals term is the key component. The contribution of the polar energies has multifold nature: in the case of upper/lower two layers (i.e.,

Table 2. Decomposition of the Average Binding Energy of Two Layers^a

unit	binding energy (kJ/mol)	upper/lower	outer	internal
X-mod1	ΔE_{vdw}	-879 ± 60	-1466 ± 38	-1529 ± 15
	ΔE_{surf}	-67 ± 5	-118 ± 3	-124 ± 5
	ΔE_{elec}	-61 ± 15	391 ± 157	530 ± 160
	ΔE_{gb}	532 ± 264	-190 ± 130	-388 ± 132
	ΔE_{np}	-946 ± 65	-1584 ± 40	-1654 ± 16
	ΔE_p	470 ± 31	201 ± 32	141 ± 35
	ΔE_{total}	-476 ± 48	-1383 ± 27	-1512 ± 32
X-mod2	ΔE_{vdw}	-1132 ± 37	-1481 ± 19	-1498 ± 24
	ΔE_{surf}	-90 ± 2	-121 ± 1	-122 ± 2
	ΔE_{elec}	-542 ± 325	334 ± 196	654 ± 151
	ΔE_{gb}	1034 ± 318	-87 ± 50	-446 ± 121
	ΔE_{np}	-1223 ± 40	-1602 ± 20	-1620 ± 25
	ΔE_p	492 ± 27	246 ± 29	208 ± 57
	ΔE_{total}	-730 ± 47	-1355 ± 37	-1412 ± 51
N-mod1	ΔE_{vdw}	-969 ± 40	-1225 ± 44	-1276 ± 37
	ΔE_{surf}	-81 ± 4	-101 ± 3	-109 ± 3
	ΔE_{elec}	-311 ± 261	607 ± 148	271 ± 152
	ΔE_{gb}	795 ± 268	-250 ± 151	-7 ± 13
	ΔE_{np}	-1050 ± 44	-1326 ± 48	-1385 ± 41
	ΔE_p	484 ± 28	357 ± 24	264 ± 29
	ΔE_{total}	-566 ± 48	-969 ± 44	-1121 ± 40
N-mod2	ΔE_{vdw}	-622 ± 34	-1263 ± 29	-1228 ± 23
	ΔE_{surf}	-57 ± 3	-108 ± 2	-107 ± 2
	ΔE_{elec}	-36 ± 29	234 ± 190	179 ± 114
	ΔE_{gb}	508 ± 280	121 ± 78	117 ± 100
	ΔE_{np}	-679 ± 37	-1371 ± 31	-1335 ± 25
	ΔE_p	472 ± 28	355 ± 36	296 ± 35
	ΔE_{total}	-207 ± 29	-1015 ± 38	-1039 ± 48

^a E_{vdw} and E_{elec} are the van der Waals and electrostatic binding terms. E_{gb} and E_{surf} are the solvation energies of polar and nonpolar residues, calculated by Amber 9 using the Generalized Born model. E_p and E_{np} are the sums of polar energy ($E_{elec} + E_{gb}$) and nonpolar energy components ($E_{vdw} + E_{surf}$), respectively. E_{total} is the sum of E_p and E_{np} . Error bars represent standard deviations.

layer stacking of L2 and L3 as shown in Figure 5), the polar solvation energy (with positive ΔE_{gb}) is unfavorable to the layer stacking, while the interpeptide electrostatic interaction (with negative ΔE_{elec}) contributes the layer stacking favorably; in the case of Outer/Internal two layers (i.e., layer growth of two zippering strands and their adjacent two strands along the fibril growth direction), the polar solvation energy (with negative ΔE_{gb}) contributes to the layer growth favorably (with the exception of N-mod2), while the interpeptide electrostatic interaction (with positive ΔE_{elec}) is unfavorable. It is also shown that the total binding energy (E_{total} , upper/lower + outer + internal) of X-mod1 (-3371 kJ/mol) is higher than that of X-mod2 (-3497 kJ/mol), and the total binding energy of N-mod1 (-2656 kJ/mol) is lower than that of N-mod2 (-2261 kJ/mol). Notably, in terms of the total potential energy, X-mod1 (-53762 kJ/mol) and N-mod1 (-52865 kJ/mol) is thermodynamically more stable than X-mod2 (-53237 kJ/mol) and N-mod2 (-52422 kJ/mol), respectively. Further, one can infer that the intramolecular energy of X-mod1 is larger than that of X-mod2, suggesting a more compact structure of

the former, which is also consistent with the larger amount of total hydrogen bonds as shown in Figure 6c.

E. The Most Likely Models. Since each experimental method (both X-ray and NMR) gives two possible models, in the following we will explore the structural differences between two models to see which one is more reasonable based on simulations. Figure 8 shows the simulated structures after 100-

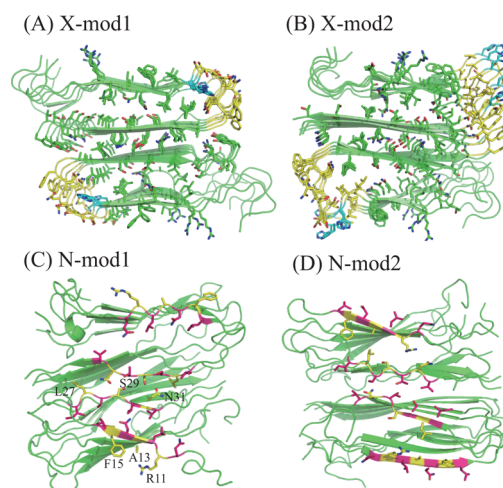


Figure 8. Final structures after 100-ns MD simulations for the protofilament in amylin fibrils. Cartoon representation of (A) X-ray model I. (B) X-ray model II. (C) NMR model I. (D) NMR model II. The side chains are shown in sticks and hydrogen atoms are hidden. Turns of the X-ray models are colored in yellow.

ns simulations. For the X-ray model I (A, X-mod1), the turn spanning SER19-GLY24 (in yellow color) is well retained. And the steric zipper conformations in both the middle and outer interfaces are well retained. While the turn structure spanning VAL17-GLY24 of X-ray model II (B, X-mod2) is severely distorted, which consequently destructs the steric zipper motif. And the β sheet adjacent to the turn is largely lost and changes into coil structures. In this sense, the model I may be a better candidate for the X-ray Eisenberg model of amylin fibril.

As for the NMR models (C and D), the simulated models show more structural flexibilities as compared with simulated X-ray models. By taking a closer look, most structural features observed in the experimental models are well maintained in simulations. For N-mod1 (C), side chains of GLN10, LEU12, ASN14, and LEU16 (in magenta) make contacts to the portion formed by residues 28–37, while side chains of ARG11, ALA13, and PHE15 (in yellow) are on the exterior of the protofilament. The side chains of LEU27, SER29, and ASN31 (in yellow) are located in the interface between the two layers of amylin molecules, while side chains of LEU26, SER 28, THR30, and VAL32 (in magenta) are in the interior of each layer. For N-mod2 (D), side chains of ARG11, ALA13, and PHE15 (in yellow) make contacts to the portion formed by residues 28–37, while side chains of GLN10, LEU12, ASN14, and LEU16 (in magenta) are on the exterior of the protofilament. The side chains of LEU26, SER28, THR30, and VAL32 are located in the interface between the two layers of amylin molecules, while side chains of LEU27, SER29, and ASN31 are in the interior of each layer. It is also noted that our simulated molecular structures of amylin protofibrils show significant left-handed twist of around 9.0° per layer.

In addition, the intramolecular distance restraints between side chains of ASN14 and ILE26 for both NMR models is well maintained for the inner layers. While the ASN14-ILE26 distances on the exterior of the protofilament increase up to 20 Å (data not shown), which shows the flexibility of the protofilament edge. This may be coincided with the structural requirement that outer strands act as growing sites. According to Padrick and Miranker's fluorescence spectroscopy measurements of amylin fibril structure, the solvent accessibility and mobility of TYR37 are reduced due to its proximity to PHE15 and/or PHE23 (estimated distances less than 11 Å) upon fibril formation.⁴² We calculated the PHE15-TYR37 and PHE23-TYR37 (between carbon α atoms) intermolecular distances as shown in Figure 9. The C α -C α distance between PHE15 and

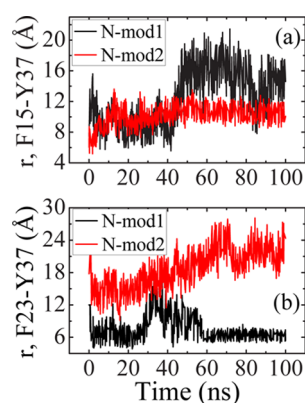


Figure 9. Time evolution of the C α -C α distances between (a) PHE15 and TYR37 and between (b) PHE15 and TYR37 during MD simulation.

TYR37 is about 14 and 10 Å for N-mod1 and N-mod2, respectively. The PHE23-TYR37 distance is roughly 6 Å for N-mod1 and 21 Å for N-mod2. Thus, the N-mod1 is more consistent with the fluorescence data.

F. Umbrella Pulling Simulation. In the following, we performed the pulling simulations on AFS3 systems of both X-ray and NMR models. The average pulling forces as a function of the center-of-mass distances between the pulling strand and the reference strand were calculated based on six trajectories for each model and are shown in Figure 10. In the initial stage of the simulations, the pulling force increases from ~ 20 kJ/mol/Å to a maximum value at the center-of-mass distance of ~ 1.5 Å. The maximum pulling force is 43.4 kJ/mol/Å and 77.3 kJ/mol/

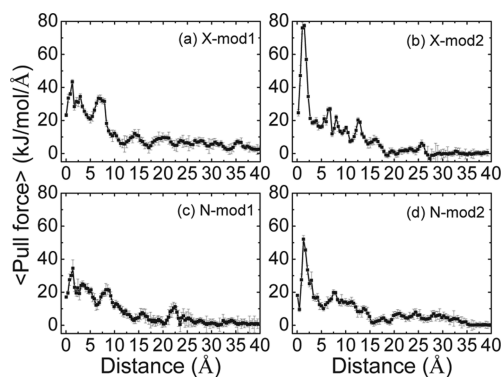


Figure 10. Average pulling forces as a function of the center-of-mass distances between the pulling strand and the reference strand.

Å for X-mod1 and X-mod2, respectively. While the maximum pulling force is 34.4 kJ/mol/Å and 52.1 kJ/mol/Å for N-mod1 and N-mod2, respectively. Thus, the average maximum pulling force for X-ray models is 17.1 kJ/mol/Å larger than that for NMR models. For all systems, the pulling forces generally decrease and fluctuate as the center-of-mass distance is larger than 1.5 Å. The pulling force decays to nearly zero when the pulling strand is pulled about 15 Å away from the reference strand.

On the basis of the pulling simulations data of AFS3 of X-mod1, we obtained the average Z-component of center-of-mass distance between each residue of the pulling strand and the reference strand at different time intervals. The result is shown in Figure 11. The results obtained from other independent

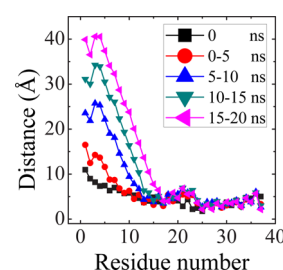


Figure 11. Z-component distance between each residue of the pulling strand and the reference strand at different time intervals for one representative trajectory.

pulling simulations show similar behaviors (data not shown). Clearly, the N-terminal segment with 17 residues (K1-V17) was much earlier pulled away from the reference strand than the C-terminal segment from H18 to Y37. This indicates that the C-terminal segment has a larger binding affinity with the preformed amylin oligomer. This may be due to the presence of more hydrophobic residues in the C-terminal strand.

The potentials of mean force (PMF, in kJ/mol) as a function of the center-of-mass distances between the pulling strand and the reference strand were calculated as shown in Figure 12, which were based on three 80-ns trajectories for each model. The energies needed to pull one β -strand away from the protofibril for X-mod1 and X-mod2 are similar, ~ 305 kJ/mol,

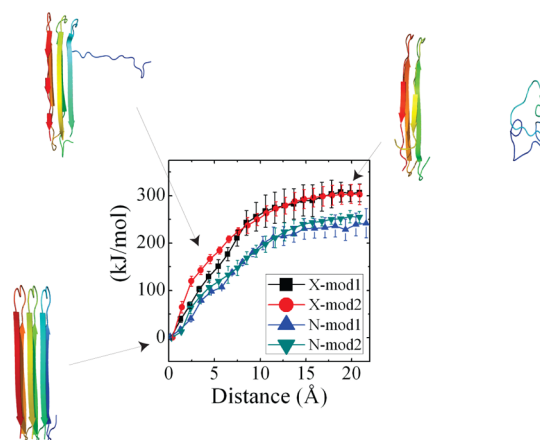


Figure 12. Potential of mean force (PMF, in kJ/mol) as a function of the center-of-mass distances between the pulling strand and the reference strand. Three representative snapshots at different pulling stages were shown as references.

while for N-mod1 and N-mod2 they are about 250 kJ/mol. A higher energy value for X-ray amylin fibril model is related to its larger amount of internal interactions as shown in Figure 6. We realize that based on such limited samplings (only three trajectories for each PMF curve), it is hard to get a really convergent pulling profile. The above results could only give a semiquantitative indicator of the mechanical stability of X-ray and NMR amylin protofibril models. In addition, three representative AFS3 structures at different pulling stages were also shown in Figure 12. In the early pulling stage, the N-terminal segment was pulled away first while the C-terminal part remained close contact with the reference strand. One can also find that the segment which was pulled away lost the β conformation, and was mainly in the random coil conformation.

IV. CONCLUSIONS

Structural models for amylin in the fibril form and for the segments of amylin in the protofibrils were recently suggested by two groups. The amylin amyloid fibril model based on NMR technique was suggested by Tycko group.⁸ Alternatively, Eisenberg group proposed a structural model based on X-ray technique.²⁷ However, there are significant differences in the two structural models which may originate from the polymorphic nature of amylin fibrils. The Tycko model apply to amylin fibrils with striated ribbon morphologies, which is comprised of untwisted, rod-like protofilaments that associate laterally into ribbons. While the Eisenberg model is possibly suitable for fibrils with an apparent axial twist. The onset of different morphologically homogeneous amylin fibrils is dependent on the unique protocol for the sample preparation. In short, it is understandable that fibrils with different morphologies legitimately have different underlying molecular structures.

To obtain further insights into the packing stability of the two different types of structural models, we performed several molecular dynamics simulations to study the amylin peptide fibril dynamically. Our results show that the protofibril models composed of a limited number of β -strands are quite stable in the 100-ns simulations, which suggests that steric zipper interactions at the β -sheet- β -sheet interface play a strong contribution to the stability of these amyloid aggregates. For both X-ray and NMR models, outer strands are more flexible coinciding with the structural requirement that outer strands act as the fibril elongation sites. Moreover, simulation results show that X-ray model is structurally more compact than NMR model and has a more intimate packing pattern, which leads to a more rigid amyloid model. As a result, the X-ray model is energetically more stable than the NMR model. Recently, amylin dimer, as the smallest functional unit of amylin fibril, whose structures, conformational properties and transitions were elaborately investigated by both experimental and simulation methods.^{43,44} Both show that amylin dimer formation is a significant early step in amyloidogenic process, and the dimer already contains the main structural elements necessary for fibril formation. Here our simulations provides structural properties for the more integrated amylin fibril of both NMR and X-ray models.

According to the clues based on previous experimental structural data, our further modeling analyses verify the most likely amylin fibril model among both NMR and X-ray models. For the X-ray model: (1) the total potential energy of X-mod1 (−53868 kJ/mol) is 460 kJ/mol on average lower than X-mod2

(−53408 kJ/mol); (2) the experimental structural features of X-mod1 are well retained in our simulated model. While some of the experimental structural features of X-mod2 are lost in the simulated model. For the NMR model: (1) N-mod1 has a higher intersheet structural complementarity than N-mod2 (see Figure 5a); (2) the total potential energy of N-mod1 (−52911 kJ/mol) is 427 kJ/mol on average lower than N-mod2 (−52484 kJ/mol); (3) N-mod1 generally matches the additional experimental distance restraints (PHE15-TYR37 and PHE23-TYR37) obtained by Padrick and Miranker's fluorescence spectroscopy measurements of amylin fibril structure,⁴² which is shown in Figure 9. In all, it is verified that N-mod1 and X-mod1 are the most possible amylin fibril models. Notably, in contrast to the NMR Tycko model of amylin fibrils, our simulated molecular structures of amylin protofibrils show significant left-handed twist of around 9.0° per layer, which however needs further experimental verification. In addition, upon further study of the force-induced dissociation of monomeric peptide from the amylin fibrils, the semiquantitative binding energy is obtained. The heterogeneity of packing pattern and the related energetic characterization is well resolved in our study.

AUTHOR INFORMATION

Corresponding Author

*E-mail: (W.X.) : wxxu@sat.ecnu.edu.cn; (Y.M.) ygmu@ntu.edu.sg.

Notes

The authors declare no competing financial interest.

ACKNOWLEDGMENTS

We thank the National Natural Science Foundation of China (Grants No. 11204083, 10974054 and 20933002). W.X.X. is grateful to the Shanghai Pujiang program (12PJ1403000) for financial support. The support of research grants, URC(RG23/11), from Nanyang Technological University and the IDA Cloud Computing Call for Project Proposals 2012 is gratefully acknowledged. The kind provision of fibril model structures by Tycko and Eisenberg is gratefully acknowledged.

REFERENCES

- (1) Kopito, R. R.; Ron, D. *Nat. Cell Biol.* **2000**, 2, E207–E209.
- (2) Goldberg, M. S.; Lansbury, P. T. *Nat. Cell Biol.* **2000**, 2, E115–E119.
- (3) Selkoe, D. J. *Nat. Cell Biol.* **2004**, 6, 1054–1061.
- (4) Luheshi, L. M.; Crowther, D. C.; Dobson, C. M. *Curr. Opin. Chem. Biol.* **2008**, 12, 25–31.
- (5) Tycko, R. *Curr. Opin. Struct. Biol.* **2004**, 14, 96–103.
- (6) Petkova, A. T.; Leapman, R. D.; Guo, Z. H.; Yau, W. M.; Mattson, M. P.; Tycko, R. *Science* **2005**, 307, 262–265.
- (7) Sawaya, M. R.; Sambashivan, S.; Nelson, R.; Ivanova, M. I.; Sievers, S. A.; Apostol, M. I.; Thompson, M. J.; Balbirnie, M.; Wiltzius, J. W.; McFarlane, H. T.; Madsen, A.; Riek, C.; Eisenberg, D. *Nature* **2007**, 447, 453–457.
- (8) Luca, S.; Yau, W. M.; Leapman, R.; Tycko, R. *Biochemistry* **2007**, 46, 13505–13522.
- (9) Shim, S. H.; Strasfeld, D. B.; Ling, Y. L.; Zanni, M. T. *Proc. Natl. Acad. Sci. U.S.A.* **2007**, 104 (36), 14197–14202.
- (10) Santini, S.; Wei, G.; Mousseau, N.; Derreumaux, P. *Structure* **2004**, 12 (7), 1245–1255.
- (11) Goldsbury, C.; Frey, P.; Olivieri, V.; Aebi, U.; Müller, S. A. *J. Mol. Biol.* **2005**, 352, 282–298.
- (12) Green, J. D.; Goldsbury, C.; Kistler, J.; Cooper, G.-J. S.; Aebi, U. *J. Biol. Chem.* **2004**, 279, 12206–12212.

- (13) Xu, W. X.; Jiang, P.; Li, W. F.; Mu, Y. G. *J. Chem. Phys.* **2009**, *130*, 164709.
- (14) Lorenzo, A.; Razzaboni, B.; Weir, G. C.; Yankner, B. A. *Nature* **1994**, *368*, 756–760.
- (15) Walsh, D. M.; Klyubin, I.; Fadeeva, J. V.; Cullen, W. K.; Anwyl, R.; Wolfe, M. S.; Rowan, M. J.; Selkoe, D. J. *Nature* **2002**, *416*, 535–539.
- (16) Kaye, R.; Head, E.; Thompson, J. L.; McIntire, T. M.; Milton, S. C.; Cotman, C. W.; Glabe, C. G. *Science* **2003**, *300*, 486–489.
- (17) Brender, J. R.; Lee, E. L.; Cavitt, M. A.; Gafni, A.; Steel, D. G.; Ramamoorthy, A. *J. Am. Chem. Soc.* **2008**, *130*, 6424–6429.
- (18) Xu, W. X.; Wei, G. H.; Su, H. B.; Nordenskiöld, L.; Mu, Y. G. *Phys. Rev. E* **2011**, *84*, 051922.
- (19) Kahn, S. E.; Andrikopoulos, S.; Verchere, C. B. *Diabetes* **1999**, *48*, 241–253.
- (20) Kahn, S. E. *Diabetologia* **2003**, *46*, 3–19.
- (21) Mirzabekov, T. A.; Lin, M. C.; Kagan, B. L. *J. Biol. Chem.* **1996**, *271*, 1988–1992.
- (22) Anguiano, M.; Nowak, R. J.; Lansbury, P. T., Jr. *Biochemistry* **2002**, *41*, 11338–11343.
- (23) Jayasinghe, S. A.; Langen, R. *Biochim. Biophys. Acta* **2007**, *1768*, 2002–2009.
- (24) Engel, M. F. M. *Chem. Phys. Lipids* **2009**, *160*, 1–10.
- (25) Gordon, D. J.; Meredith, S. C. *Biochemistry* **2003**, *42*, 475–485.
- (26) Sato, T.; Kienlen-Campard, P.; Ahmed, M.; Liu, W.; Li, H.; Elliott, J.; Aimoto, S.; Constantinescu, S.; Octave, J.; Smith, S. *Biochemistry* **2006**, *45*, 5503–5516.
- (27) Wiltzius, J.-J. W.; Sievers, S. A.; Sawaya, M. R.; Cascio, D.; Popov, D.; Riekel, C.; Eisenberg, D. *Protein Sci.* **2008**, *17*, 1467–1474.
- (28) Esposito, L.; Pedone, C.; Vitagliano, L. *Proc. Natl. Acad. Sci. U.S.A.* **2006**, *103*, 11533–11538.
- (29) Horn, A. H. C.; Sticht, H. *J. Phys. Chem. B* **2010**, *114*, 2219–2226.
- (30) Park, J.; Kahng, B.; Hwang, W. *PLoS Comput. Biol.* **2009**, *5*, e1000492.
- (31) Wu, C.; Bowers, M. T.; Shea, J.-E. *PLoS Comput. Biol.* **2010**, *6*, e1000693.
- (32) Jorgensen, W. L.; Maxwell, D. S.; Tirado-Rives, J. *J. Am. Chem. Soc.* **1996**, *118*, 11225–11236.
- (33) Berendsen, H. J. C.; van der Spoel, D.; van Drunen, R. *Comput. Phys. Commun.* **1995**, *91*, 43–56.
- (34) Hess, B.; Bekker, H.; C., B. H. J.; Fraaije, J. G. E. M. *J. Comput. Chem.* **1997**, *18*, 1463–1472.
- (35) Darden, T.; D. Y.; Pedersen, L. *J. Chem. Phys.* **1993**, *98*, 10089–10092.
- (36) Kabsch, W.; Sander, C. *Biopolymers* **1983**, *22*, 2577–2637.
- (37) Case, D. A.; Cheatham, T. E., III; Simmerling, C. L.; Wang, J.; Duke, R. E.; Luo, R.; Merz, K. M.; Pearlman, D. A.; Crowley, M.; Walker, R. C.; Zhang, W.; Wang, B.; Hayik, S.; Roitberg, A.; Seabra, G.; Wong, K. F.; Paesani, F.; Wu, X.; Brozell, S.; Tsui, V.; Gohlke, H.; Yang, L.; Tan, C.; Mongan, J.; Hornak, V.; Cui, G.; Beroza, P.; Mathews, D. H.; Schafmeister, C.; Ross, W. S.; Kollman, P. A. *Amber9*; University of California, San Francisco: San Francisco, CA, 2006.
- (38) Onufriev, A.; Bashford, D.; Case, D. A. *Proteins* **2004**, *55*, 383–394.
- (39) Andricioaei, I.; Karplus, M. *J. Chem. Phys.* **2001**, *115*, 6289–6292.
- (40) Xu, W. X.; Jiang, P.; Mu, Y. G. *J. Phys. Chem. B* **2009**, *113*, 7308–7314.
- (41) Lawrence, M. C.; Colman, P. M. *J. Mol. Biol.* **1993**, *234*, 946–950.
- (42) Padrick, S. B.; Miranker, A. D. *J. Mol. Biol.* **2001**, *308*, 783–794.
- (43) Dupuis, N. F.; Shea, J. E.; Bowers, M. T. *J. Am. Chem. Soc.* **2011**, *133*, 7240–7243.
- (44) Laghaei, R.; Mousseau, N.; Wei, G. H. *J. Phys. Chem. B* **2011**, *115*, 3146–3154.